Large-scale multidisciplinary design optimization of a virtual-telescope CubeSat swarm

Victor Gandarillas * and John T. Hwang †
University of California San Diego

CubeSats are small satellites that offer a low-cost alternative to larger spacecraft for space research missions. Lower costs facilitate development of distributed platforms for a more diverse set of potential missions. Due to the time constraints of typical one-to-three-year design cycles, design decisions for CubeSats are often made based on subjective experience and intuition rather than thorough and systematic design studies. However, distributed platforms require a more robust and efficient approach to making design decisions to fit within short design cycles. Previously, large-scale multidisciplinary design optimization has been applied to the design and operation of a single-CubeSat; however has not yet been applied to distributed platforms. One example of a distributed platform is a virtual telescope, where the optics and detector of the telescope each reside on a different spacecraft. This paper applies large-scale multidisciplinary design optimization to the vehicle design and trajectory optimization of a mission with two CubeSats flying in formation to form a virtual telescope. We develop a novel relative orbit model that avoids introducing truncation errors and demonstrate the successful application of multidisciplinary design optimization to the design of a virtual telescope.

I. Introduction

SmallSats and CubeSats are classes of miniature satellites that are becoming increasingly popular for scientific and commercial missions due to their low cost and versatility. They have been used for a variety of missions, including Earth observation and scientific research. They also offer a relatively affordable alternative to traditional large-scale missions and allow for increased frequency of launches. In recent years, SmallSats and CubeSats have seen a significant growth in mission diversity, including Earth observation, planetary exploration, space technology development, and scientific research.

A diversity of mission requirements has led to a diversity of SmallSat and CubeSat designs. The SmallSat X-ray Quantum Calorimeter Satellite (XQCSat) [1, 2] is designed to perform X-ray spectroscopy. CubeSats such as the Radiometer Assessment using Vertically Aligned Nanotubes (RAVAN) [3], designed to measure the Earth's outgoing radiation, and the Lunar Flashlight [4], designed to search for ice on the Moon's surface, also showcase the diversity of satellite designs.

One advantage of SmallSats and CubeSats is their small size, which makes them easy to launch and allows for multiple spacecraft to be launched at once. Some satellite missions require multiple spacecraft to form a distributed platform and fly in formation. The TerraSAR-X and Tandem-X (TerraSAR-X add-on for Digital Elevation Measurement) [5] spacecraft use Synthetic Aperture Radar (SAR) to produce high-resolution images of the Earth's surface and generate a Digital Elevation Model (DEM) of the Earth's surface. The TechSat-21 [6] was a technology demonstration mission focused on demonstrating new technologies for formation flight. TanDEM-X and TechSat-21 are both remote sensing systems, but SmallSats have filled the need for formation flight beyond Earth orbit as well. The Double Asteroid Redirection Test (DART) [7, 8] was a technology demonstrator aimed at redirecting near-Earth objects (NEOs) that successfully redirected an asteroid.

Virtual telescopes represent another application of SmallSats and CubeSats, which leverage formation-flying to observe celestial objects. These platforms offer a cost-effective alternative to traditional telescopes, which can be expensive to build and maintain. Virtual telescopes are formed from SmallSats, such as the Miniature Distributed Occulter Telescope (mDOT) [9], Virtual Telescope for X-ray Observations (VTXO) [10, 11, 11, 12], and Proba-3 [13, 14] missions, or CubeSats, such as the VIrtual Super-resolution Optics with Reconfigurable Swarms (VISORS) [15–17].

Multidisciplinary design optimization (MDO) is the use of numerical optimization to generate designs for engineering systems that involve multiple subsystems or disciplines [18]. Many MDO problems have objective and constraint

*Ph.D. Candidate, Department of Mechanical and Aerospace Engineering, AIAA Member
†Assistant Professor, Department of Mechanical and Aerospace Engineering, AIAA Member

functions that are continuous and differentiable in the design variables. These problems are also known as nonlinear programs (NLPs). Gradient-based approaches to solving NLPs scale better with the number of design variables than gradient-free approaches. A disadvantage of gradient-based approaches is that they require derivative information from the model of the system, which can be difficult to implement for large-scale multidisciplinary systems, especially when there is coupling across disciplines. Computing exact derivatives for models with multiple disciplines often relies on computational architectures [19] and software frameworks [20, 21] that facilitate multidisciplinary model definition, evaluation, and derivative computation. The large-scale MDO of a CubeSat mission has been demonstrated previously with the CubeSat investigating Atmospheric Density Response to Extreme driving (CADRE), a remote-sensing Earth observation mission [22]. The CADRE MDO algorithm involved several disciplines: communication, battery, thermal, electrical, attitude dynamics, and orbit dynamics. These disciplines are all tightly coupled, and due to the simulation of 9 orbits, the NLP contains tens of thousands of variables.

This paper is concerned with a mission inspired by the VISORS mission. VISORS is a CubeSat swarm mission with the objective of observing active solar regions with a virtual telescope, where the optics and detector reside on separate spacecraft [15–17]. As such, VISORS imposes tight alignment and separation constraints during the observation phase of the mission, which couples the dynamics of all the CubeSats in the swarm. Major challenges present themselves with a virtual telescope that are not present with a single-CubeSat mission. First, tight alignment and pointing constraints are imposed on the swarm. These constraints are on the order of tens millimeters while the positions of the spacecraft relative to the center of the Earth are on the order of thousands of kilometers, requiring an approach that captures multi-scale effects without introducing numerical error.

This paper applies MDO to the design of a virtual telescope mission with two CubeSats flying in formation. The problem definition uses a relative orbit model that captures orbit perturbations and whose numerical accuracy is robust to the size of the orbit of the spacecraft and the number of spacecraft in a swarm. The successful design of a virtual telescope mission demonstrates MDO as a practical, scalable approach to solving spacecraft mission design problems involving swarms flying in formation. The paper is organized as follows. Section III presents an overview of the mission design. Section IV presents an overview of the spacecraft discipline models. Section VI presents results for this study. Section VII concludes the paper.

II. Approach

This section presents the approach for solving the problem of designing a virtual telescope using multidisciplinary design optimization (MDO). A virtual telescope is a telescope where the main components such as the optics and detector reside on different spacecraft (Figures 2, 3). Designing a virtual telescope is a large-scale MDO problem with complex interactions across spacecraft and spacecraft subsystems. The interactions between the spacecraft models are the alignment, separation, and pointing constraints during the observation phase of the mission. The telescope formation places constraints on the interactions between the spacecraft, and power requirements lead to constraints on variables within the individual spacecraft subystems.

The large number of variables and complex interaction between the spacecraft disciplines and the spacecraft subsystem disciplines present a challenge to finding an optimal design for a virtual telescope mission. Therefore, an approach that handles a large number of variables and complex interactions between disciplines, and is necessary to achieve an optimal design for a virtual telescope mission.

The approach used in this paper is a gradient-based approach that solves the trajectory optimization and spacecraft sizing problems. Gradient-based approaches are preferable to gradient-free approaches when the problem objective and constraints are continuous and differentiable functions of the design variables because they converge to a solution much more quickly than gradient-free methods. Since gradient-free methods need to explore the entire design space, the number of function evaluations required for convergence grows as an exponential function of the number of the design variables. Alternatively, gradient-based methods exhibit quadratic rate of convergence near a local optimum. It is important to note that neither gradient-free nor gradient-based methods guarantee convergence to a global optimum.

Gradient-based methods present their challenges, however. First, gradient-based methods can only be applied to problems where the objective and constraint functions are continuous and differentiable in the design variables. Second, computing derivatives for all the functions in the system model scales poorly in terms of development time and effort unless a framework provides some level of automation for computing derivatives. Third, computing derivatives for systems with coupled variables can be memory intensive if not implemented carefully. Fourth, some discipline models can be discrete functions, which prevent the use of gradient-based methods unless a well-justified continuous and differentiable approximation to the discrete model can be incorporated into the system model.

The first obstacle is that not all design variables in the optimization problem are continuous quantities, and the problem must be modified in order to use a gradient-based approach. Four design variables are integer design variables: the number of battery cells connected in series, and the number of battery cells connected in parallel, for each of the two spacecraft (Table 4). Integer design variables are discrete quantities, so constraints that depend on the integer design variables are not continuous and differentiable over all the design variables. The number of battery cells connected in series and the number of battery cells connected in parallel are treated as real numbers, the solution is rounded to the nearest integer, and the problem is solved once more with the integer variables fixed. We can use a branch and bound algorithm, branching on the variables n_s, n_p for each spacecraft.

The adjoint method overcomes the second and third obstacles to using a gradient-based approach efficiently by computing derivatives for large-scale, coupled systems. The cost of adjoint-based derivative computation is largely independent of the number of inputs (design variables) when the number of inputs is greater than the number of outputs (objective and constraints) [23]. An advantage that adjoint-based derivative computation has over other methods such as automatic differentiation is that the coupled systems of equations are converged prior to applying the reverse chain rule instead of "unrolling" for loops, introducing memory overhead. Although the cost of the adjoint method does not scale with the number of design variables, it does scale with the number of constraint variables. Each constraint increases the size of the system Jacobian by the number of time steps where the constraint is enforced, which leads to slower convergence when solving the optimization problem. Constraints that are enforced at all time steps may be aggregated into one constraint. To reduce the size of the problem, the constraints at all time steps are aggregated into a single inequality constraint using the Kresselmeier-Steinhausser (KS) function [24]. The KS function is a continuous and differentiable function that aggregates constraints across all time steps into one constraint by approximating the maximum value of an array. The KS function is given by

$$\mathrm{KS}(x) = g_{i,max}(x) + \frac{1}{\rho} \ln \sum_i \exp[\rho(g_{i(x)} - g_{i,max}(x))], \quad (1)$$

where $g_i(x)$ is the i^{th} value of the function $g(x)$, $g_{i,max}(x)$ is the maximum value of the function $g(x)$, ρ is a smoothing parameter. The value of ρ is problem-dependent. As ρ approaches zero, the KS function overestimates the maximum. By enforcing an upper (lower) bound on the maximum (minimum) value of an array, the KS function encourages the optimizer to resolve largest infeasibilities first.

The implementation overhead of applying the adjoint method is also a factor in the decision to use the adjoint method to compute derivatives. Fortunately, software frameworks such as OpenMDAO [20] and the Computational System Design Language (CSDL) [21] are available to facilitate implementation of derivatives for large-scale, making gradient-based optimization accessible to users. In this paper, the MDO problem is defined in CSDL. CSDL uses a compiler that fully automates adjoint-based derivative computation. The key advantages of using CSDL in this paper are that (1) CSDL provides a natural way to compose models and their interactions, and (2) CSDL fully automates derivative computation for large-scale, coupled systems. CSDL is used to define the optimization problem and the SQP solver SNOPT [25] is used to solve the optimization problem.

The fourth challenge of applying gradient-based methods to optimization problems arises when physics-based models are not available, and system modelers only have access to experimental data. This challenge is overcome by training continuous and differentiable surrogate models on discontinuous data. All surrogate models in this paper rely on regularized minimal-energy tensor-product B-splines (RMTB) [26]. RMTB models provide fast predictions for low-dimensional models and do not suffer from numerical issues when trained using large data sets.

III. Mission Overview

This section provides an overview of the mission to which the approach described in Section II is applied. Section IV presents overviews of each discipline involved in the model. The mission under consideration is inspired by the Virtual Super-resolution Optics with Reconfigurable Swarms (VISORS), whose primary mission objective is to make high resolution images of active solar regions to enable testing fundamental theories of coronal heating on the Sun [15].

A virtual telescope is a compelling concept for space-based telescope design. A space-based virtual telescope is a telescope comprised of more than one spacecraft, each carrying different elements of the telescope. Because a virtual telescope is not restricted to house the components on a single spacecraft, the mass of the telescope remains relatively constant as the dimensions of the telescope increase.

Greater observational capability generally requires larger telescopes capable of collecting more light and/or focusing at greater distances. The dimensions of the telescope depend on the in-flight formation than on the size of the individual spacecraft. To ensure that launch costs scale well with the size of the telescope, the trajectory must be chosen to minimize total propellant used.

Each orbit contains an observation and standby phase (Figure 1). In the observation phase, the telescope makes scientific observations of the corona. In order to form a telescope, the spacecraft must satisfy tight alignment and separation constraints during the observation phase, obtaining accurate measurements of the target area on the corona. In the standby phase, the spacecraft must satisfy power requirements. The virtual telescope in this study is comprised of two CubeSats, one carrying the optics portion of the telescope, and the other carrying the detector used to record images. Each CubeSat is referred to by the scientific equipment it carries: the spacecraft carrying the optics is called the Optics Spacecraft (OSC), and the spacecraft carrying the detector is called the Detector Spacecraft (DSC). The OSC will be equipped with a photon sieve, which will focus light on the DSC at a higher resolution than possible with traditional optics.

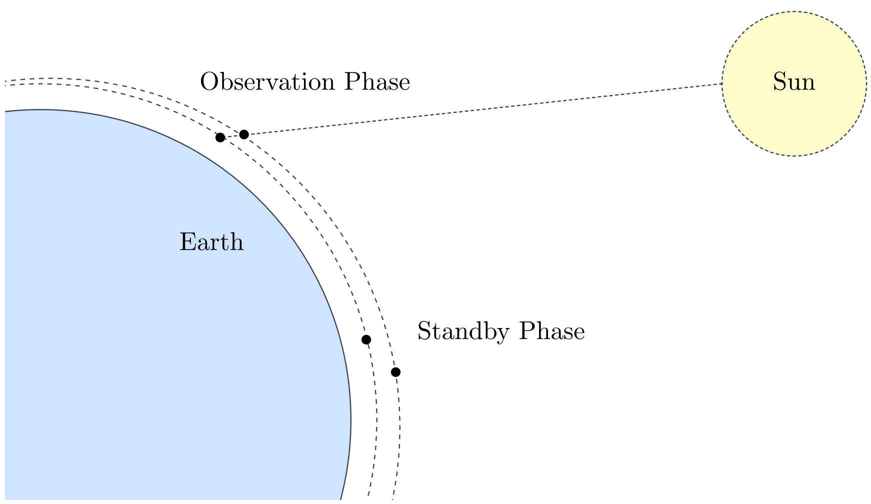

Figure 1 Concept of operations for the virtual telescope based on the Virtual Super-resolution Optics with Reconfigurable Swarms (VISORS) mission.

Each observation requires that the OSC and DSC maintain telescope formation for one 10 s interval per orbit. During the observation phase, the spacecraft are required to maintain a nominal separation of 40 m±15 mm, alignment within 18 mm, and pointing error below 90 arcsec (Figure 2).

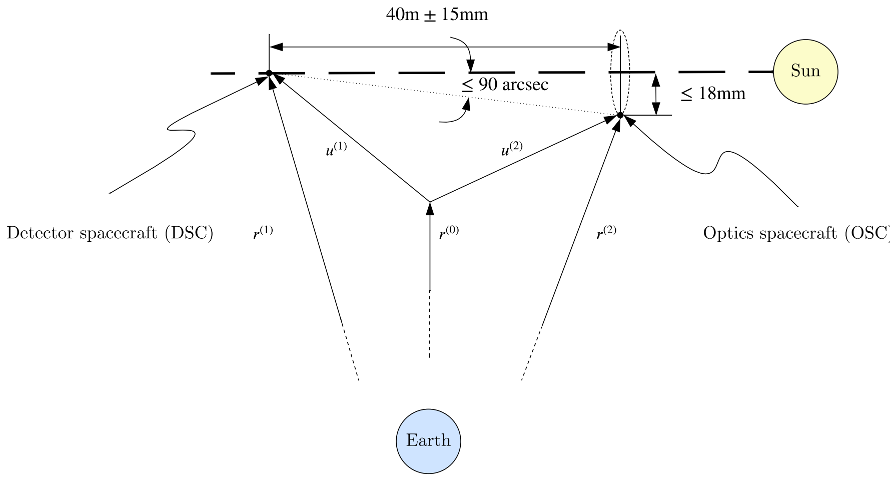

Figure 2 Spacecraft with positions $r^{(i)}$ relative to Earth, and positions $u^{(i)}$ relative to reference orbit $r^{(0)}$ with alignment, separation, and pointing constraints as listed in Table 3

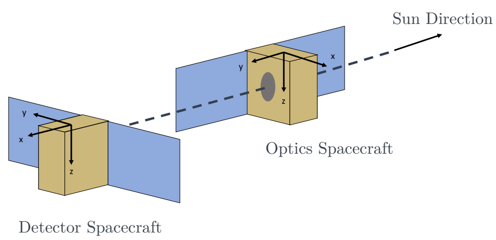

Figure 3 CubeSats shown in their attitude configuration during observations of the Sun. The body reference frame of each spacecraft is shown. The Detector Spacecraft is oriented such that light from the Sun enters the detector and the Optics Spacecraft is oriented such that light from the Sun passes through the optics onboard the Optics Spacecraft.

IV. Discipline Models

A. Propulsion

Each CubeSat has thrusters to control its translational motion Omnidirectional thrust can be achieved by installing six thrusters are installed on each CubeSat along both directions in each of the three axes. (Cite a VISORS paper that shows this configuration.) For simplicity, the thrust design variables are defined in the ECI frame. The thrust in the body frame can be computed via a transformation by applying a rotation matrix to the thrust at each time step. The thrusters are cold gas thrusters. Total propellant mass is set to 1 kg, and total propellant used is minimized. By minimizing total propellant mass used, the lifetime of the spacecraft is maximized. how is the absolute value calculated?

Each CubeSat is equipped with thrusters to control the translational motion. The propulsion discipline for each CubeSat is modeled such that each CubeSat has omnidirectional translational control. Omnidirectional translational control requires six thrusters firing in the direction of the positive and negative directions along each axis of the body frame. For simplicity, the thrust over time $F_{\text{thrust},i}(t), i \in \{1, 2, 3\}$ is defined in the ECI frame, which is the same frame used in the orbit dynamics model (Section IV.B), and can be translated to the body frame to model the amount of force that each thruster imparts tot he spacecraft.

The thrusters used for this mission are cold gas thrusters using R236FA as the propellant, in accordance with the

Table 1 CubeSat Design Parameters

Parameter	Value
Tank Pressure	100 psi
Propellant Mass	0.17 kg
Battery Chemistry	Li-ion
Propellant	R236FA

VISORS concept of operations [15]. Table 1 shows the complete set of parameters for each CubeSat. The values of these parameters are fixed throughout the optimization; i.e. they are not design variables. The initial propellant mass m_0 for each CubeSat is a design variable in the optimization problem. The propellant mass evolves over time according to the differential equation

$$\dot{m}(t) = -\frac{\sum_{i=1}^{3} |F_{\text{thrust},i}(t)|}{g_0 I_{\text{sp}}}, \tag{2}$$

where g_0 is the acceleration due to gravity at sea level and I_{sp} is the specific impulse of the cold gas thruster. The absolute value is used to capture the fact that propellant is always used regardless of the direction of thrust. For gradient-based optimization, however, the absolute value function is discontinuous at zero, so the thrust design variables are split into a set of positive and negative values.

B. Orbit Dynamics

This section presents a relative orbit model that can be used for optimizing trajectories of spacecraft swarms subject to millimeter-level constraints. The new orbit model can be used within a multidisciplinary design optimization (MDO) framework to design swarm missions with any number of spacecraft.

The key challenge of trajectory optimization with millimeter-level constraints lies in computing the positions of the spacecraft with the numerical precision necessary for solver convergence. In Low Earth Orbit (LEO), the equations of motion for the spacecraft orbits are functions of the positions of spacecraft relative to the Earth, which are on the order of thousands of kilometers, while the constraints on the dimensions of the swarm formation are on the order of tens of millimeters. This is a difference of eight orders of magnitude.

When integrating the equations of motion of the spacecraft positions relative to the center of the Earth, large differences in orders of magnitude introduce truncation errors, rendering numerical optimization impossible. As a result, the optimizing solver cannot update the constraint values with the required level of precision to converge to a feasible solution.

A model of the orbits of the spacecraft in the swarm that does not introduce truncation errors is developed to make numerical optimization of the swarm design problem possible and presented as follows. To reduce the relative orders of magnitude between the constraint values, design variable values, and intermediate state variable values, a trajectory for each spacecraft relative to a reference orbit is used. The position of the i^{th} spacecraft $r^{(i)}(t)$ (Figure 2) is given by

$$r^{(i)} = r^{(0)} + u^{(i)}, \tag{3}$$

where $r^{(0)} \in \mathbb{R}^3$ is a reference orbit position, and $u^{(i)} \in \mathbb{R}^3$ is the position of the i^{th} spacecraft relative to the reference orbit. The equations of motion for the spacecraft relative to the reference orbit $r^{(0)}$ are given by

$$\ddot{u}^{(i)} = \ddot{r}^{(i)} - \ddot{r}^{(0)}. \tag{4}$$

The orbit dynamics of the reference orbit $r^{(0)}$ and the spacecraft positions relative to the center of the Earth $r^{(i)}$ are modeled by

$$
\begin{aligned}
\ddot{r} = -\frac{\mu}{r^3} r - \frac{3\mu J_2 R_e^2}{2r^5} & \left[\left(1 - \frac{5r_z^2}{r^2} \right) r + 2r_z \hat{z} \right] \\
- \frac{5\mu J_3 R_e^3}{2r^7} & \left[\left(3r_z - \frac{7r_z^3}{r^2} \right) r \right. \\
& \left. + \left(3r_z - \frac{3r^2}{5r_z} \right) r_z \hat{z} \right] \\
+ \frac{15\mu J_4 R_e^4}{8r^7} & \left[\left(1 - \frac{14r_z^2}{r^2} + \frac{21r_z^4}{r^4} \right) r \right. \\
& \left. + \left(4 - \frac{28r_z^2}{3r^2} \right) r_z \hat{z} \right].
\end{aligned}
\tag{5}
$$

The J_2, J_3, and J_4 terms capture perturbations that affect the orbit on the order of months, where the orbital period for Low Earth Orbit (LEO) is generally on the order of 90 minutes. The use of multidisciplinary design optimization (MDO) will capture these effects across multiple time scales, as well as the effect of rotating the orbit plane on power generation. Note that if $\ddot{r}^{(i)}$ and $\ddot{r}^{(0)}$ are modeled using Equation (5), then $\ddot{r}^{(0)}$ is a function of $r^{(0)}$, and $\ddot{r}^{(i)}$ is a function of $r^{(i)} = u^{(i)} + r^{(0)}$. Expanding Equation (4) by modeling $\ddot{r}^{(0)}$ and $\ddot{r}^{(i)}$ using Equation (5) leads to

$$
\begin{aligned}
\ddot{u} = -\frac{3\mu J_2 R_e^2}{2\|r^{(0)}\|^5} & \left[\left(1 - \frac{5(r_z^{(0)} + u_z)^2}{\|r^{(0)}\|^2} \right) u + 2u_z \hat{z} \right] \\
- \frac{5\mu J_3 R_e^3}{2\|r^{(0)}\|^7} & \left[\left(3(r_z^{(0)} + u_z) - \frac{7(r_z^{(0)} + u_z)^3}{\|r^{(0)}\|^2} \right) u \right. \\
& \left. + \left(6r_z^{(0)} + 3u_z \right) u_z \hat{z} \right] \\
+ \frac{15\mu J_4 R_e^4}{8\|r^{(0)}\|^7} & \left[\left(1 - \frac{14(r_z^{(0)} + u_z)^2}{\|r^{(0)}\|^2} + \frac{21(r_z^{(0)} + u_z)^4}{\|r^{(0)}\|^4} \right) u \right. \\
& \left. + \left(4 - \frac{28}{3\|r^{(0)}\|^2} (3(r_z^{(0)})^2 + 3r_z^{(0)} u_z + u_z^2) \right) u_z \hat{z} \right].
\end{aligned}
\tag{6}
$$

Then the $\ddot{u}^{(i)}$ in Equations (4), (6) is a function of $r^{(0)}$, and $u^{(i)}$ with no explicit dependence on $r^{(i)}$. Since the $r^{(0)}$ do not depend on any design variables, the magnitudes of the $r^{(0)}$ have no impact on the precision of the constraints imposed on the $u^{(i)}$. Furthermore, the reference orbit $r^{(0)}$ can be computed once prior to optimization, reducing computation time each time the model is evaluated. Figure 4 shows two trajectories of free-flying spacecraft relative to a reference orbit. These trajectories are computed by integrating Equation (4) for each spacecraft using initial conditions corresponding to the desired orbit in Table 2.

Table 2 VISORS orbit requirements, preferred orbit, and orbit insertion tolerance

Orbital Parameter	Requirement	Preferred	Tolerance
Altitude	450-600km	500km	± 50km
Inclination	≥ 30°	97.4°	±0.2°
Eccentricity	≤ 0.1	0.001	±0.01

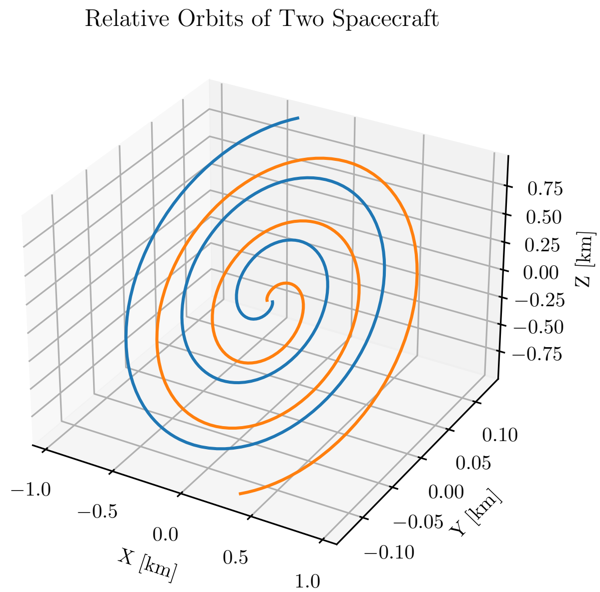

Figure 4 Positions of two free-flying spacecraft relative to a sun-synchronous reference orbit over 3 orbits around the Earth. The initial conditions of the spacecraft are offset from the initial condition for the reference orbit by 20 m in the $+x$ and $-x$ directions. Coordinates are in the Earth-Centered Inertial (ECI) frame of reference.

The desired orbit parameters in Table 2 are based on the orbit requirements for the VISORS mission [16]. The mission requirements call for a telescope maintaining a sun-synchronous orbit due to the ease of accessibility by secondary payloads and the slow and predictable change in beta angle throughout the year [17].

C. Attitude Dynamics and Control

Both the observation phase and standby phase of the orbit impose requirements on the spacecraft behavior that determines the attitude profiles of the spacecraft. The pointing requirements imposed on the spacecraft to maintain the telescope formation dictate the attitude profile during the observation phase. Power requirements imposed on the electrical power subsystem to maximize mission lifetime constrain the attitude profile throughout the standby phase. In this paper, the Euler angles (roll, pitch, and yaw) defining the attitude of each spacecraft are optimized to satisfy the individual spacecraft pointing and sizing constraints. During the observation phase of the orbit, the spacecraft must point their instruments toward the Sun to record observations, and the battery state of charge must remain within 20-95% throughout the orbit to minimize battery degradation while maintaining a power balance. The battery and solar power models are presented in Sections IV.F and IV.E, respectively. The reaction wheels controlling the attitude of the spacecraft are also limited limited to a maximum torque and power of 0.004 Nm and 1 W, respectively to match the Blue Canyon Technologies RWP015 reaction wheel specifications [27]. The reaction wheel constraints, listed in Table 4, are enforced using a KS function (1) in Section II.

First, a rotation matrix is constructed to transform coordinates from the Earth-Centered Inertial (ECI) frame to the spacecraft body frame by

$$R_{B/I} = \begin{bmatrix} c_\theta c_\psi & c_\theta s_\psi & -s_\theta \\ s_\phi s_\theta c_\psi - c_\phi s_\psi & s_\phi s_\theta s_\psi + c_\phi c_\psi & c_\theta s_\phi \\ c_\phi s_\theta c_\psi + s_\phi s_\psi & c_\phi s_\theta s_\psi - s_\phi c_\psi & c_\theta c_\phi \end{bmatrix},$$

where $s_{(\cdot)}$ and $c_{(\cdot)}$ denote the sine and cosine of an angle, respectively, and ψ, θ, ϕ are roll,pitch, and yaw, respectively. The rotational dynamics of the spacecraft (in the body frame) are given by

$$\dot{L}_B = \tau_B + \tau_{RW} + \omega_B \times (L_{RW}) + \tau_g = 0,$$

where L_B is the angular momentum of the spacecraft, $\tau_{RW} = J_{RW} \cdot \dot{\omega}_{RW}$ is the torque imparted to the spacecraft by reaction wheels, and τ_g is the torque imparted to the spacecraft by the Earth's gravity. The torque $\tau_B = J_B \cdot \dot{\omega}_B + \omega_B \times (J_B \cdot \omega_B) + \tau_g$, The torque τ_g is given by

$$\tau_{g,x}(t) = -3(J_{B,y} - J_{B,z})\Omega(t)^2 (R_{B/A})_{21}(R_{B/A})_{31} \tag{7}$$

$$\tau_{g,y}(t) = -3(J_{B,z} - J_{B,x})\Omega(t)^2 (R_{B/A})_{31}(R_{B/A})_{11} \tag{8}$$

$$\tau_{g,z}(t) = -3(J_{B,x} - J_{B,y})\Omega(t)^2 (R_{B/A})_{11}(R_{B/A})_{21}, \tag{9}$$

where $\Omega(t)$ is the osculating angular speed of the spacecraft position in the orbit and $R_{B/A}$ is the rotation matrix from the orbit frame to the body frame given by

$$R_{B/A} = \begin{bmatrix} \hat{r}^T \\ ((\hat{r} \times \hat{v}) \times \hat{r})^T \\ (\hat{r} \times \hat{v})^T \end{bmatrix}.$$

Using a constant orbit angular speed models the attitude dynamics under the assumption that the orbit is circular, while using the osculating orbit angular speed takes into account the effect of orbit perturbations.

The angular velocity of the spacecraft ω_B is known from computing $\omega_B^\times = \dot{R}_{B/I}(R_{B/I})^T$, where $\dot{R}_{B/I}$ is computed using via finite differences. The angular acceleration of the spacecraft $\dot{\omega}_B$ is also computed via finite differences. The resulting ordinary differential equation

$$\dot{\omega}_{RW} = J_{RW}^{-1}(\omega_B \times (J_{RW} \cdot \omega_{RW}) - \tau_B)$$

is then integrated to obtain reaction wheel angular velocities $\omega_{RW}(t)$. Once the reaction wheel angular velocities are computed, the reaction wheel torques $\tau_{RW}(t)$ are computed by

$$\tau_{RW} = J_{RW}\dot{\omega}_B \tag{10}$$

$$P_{RW} = \tau_{RW}\omega_B. \tag{11}$$

D. Solar Illumination

The amount of power generated by the solar arrays depends on the amount of solar illumination. The solar illumination is a function of the orientation of the spacecraft relative to the Sun, placement of the solar arrays on the spacecraft, and the dimensions of the solar arrays. To compute the solar illumination, a ray tracing algorithm provided by TALSO [28]. Figure 5 shows training and test data for the solar arrays used in this study.

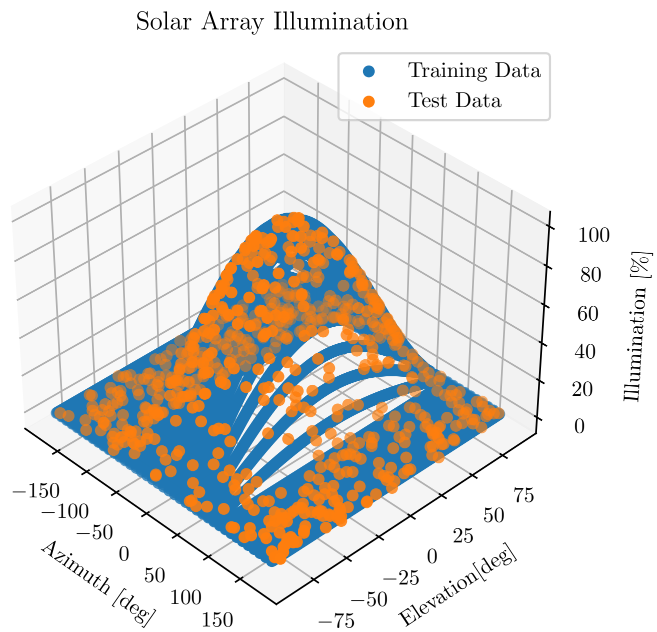

Figure 5 Solar illumination as a percent of the area of solar arrays illuminated as a function of azimuth and elevation. The training data is generated using a ray tracing algorithm provided by TALOS[28].

The percent solar illumination depends on the position of the CubeSats in the orbit as well as its attitude. For each CubeSat, a line of sight indicator is also computed as shown in Figure 6. The sun line of sight indicator is defined as

$$LOS_s = \begin{cases} 1 & \hat{r}_{b/e} \cdot \hat{r}_{s/e} \geq 0 \\ \begin{cases} 1, & d_s > R_e \\ 3\eta^2 - 2\eta^2, & \alpha R_e < d_s < R_e \\ 0, & d_s < \alpha R_e \end{cases}, & \hat{r}_{b/e} \cdot \hat{r}_{s/e} < 0 \end{cases},$$

where

$$d_s = \|\hat{r}_{b/e} \times \hat{r}_{s/e}\|_2 \quad \eta = \frac{d_s - \alpha R_e}{R_e - \alpha R_e}.$$

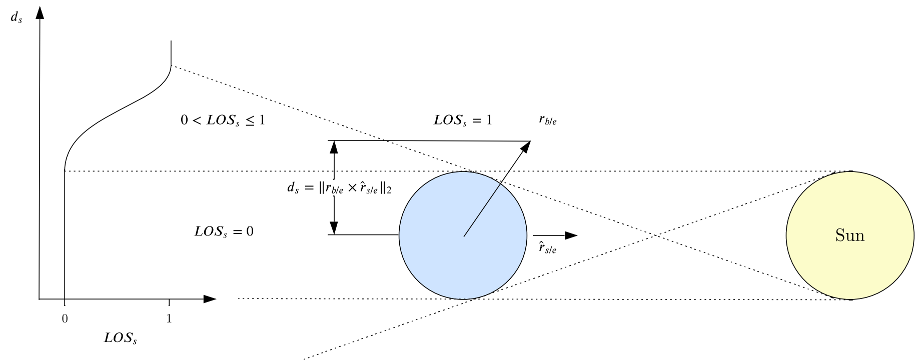

Figure 6 Schematic of Sun line-of-sight (LOS_s) variable indicating when each spacecraft has a line of sight to the Sun. When $LOS_s = 0$, the spacecraft is hidden behind the Earth's shadow, and when $LOS_s = 1$, the spacecraft has a line of sight to the Sun. A gradient-based approach to optimization cannot handle the discontinuous jump between the two states, so a continuous and differentiable function is used. The continuous and differentiable function is also physically justified by modeling the umbra and penumbra effects of the Earth's shadow.

E. Solar Power

The solar power discipline models the power supplied by the solar arrays on the spacecraft. For this study, the solar power discipline described in [29] is used to model the current and voltage of the solar arrays. The solar array current is a design variable in the optimization.

$$
\begin{aligned}
V(I) &= \frac{V_{OC} + V_0}{2} + \frac{V_{OC} - V_0}{2} \tanh\left(b(I - I_{sc}) + \operatorname{arctanh}\left(\frac{V_0 + V_{OC}}{V_0 - V_{OC}}\right)\right) \\
b &= \frac{1}{V_{OC} - V_0} \frac{dV}{dI} \\
\frac{dV}{dI} &= -\frac{V_T}{V_T + I_{sat} Rsh} R_{sh} \\
V_{OC} &= 1.1 V_T \ln \frac{V_T}{I_{sat} R_1} \\
R_1 &= 1
\end{aligned}
\tag{12}
$$

The solar array discipline in [29] is an explicit approximation of the model described in [30]. Figure 7 shows the I-V curve for the solar arrays. The constants and variables in 12 are listed in [31].

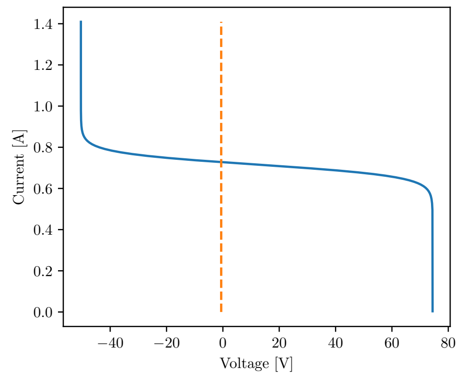

Figure 7 I-V curve for solar arrays

F. Battery Model

Each CubeSat stores energy in a battery pack to power its subsytems. The spacecraft subsystems drain power from the battery pack, limiting its use. Each CubeSat is equipped with solar arrays to recharge its batteries using energy from the Sun in flight. Using rechargeable batteries greatly extends the life of the mission. Charging and discharging the batteries too much can lead to premature degradation, however. To maximize the lifetime of the CubeSats, the state of charge of the batteries is constrained to be within 20-95%. (Something about constant OCV) The attitude profile must be designed to satisfy this constraint so that the solar arrays are oriented toward the Sun during the standby phase long enough to store the energy required to power the spacecraft subsystems, but not so long that the batteries are overcharged.

Each CubeSat needs to be able to store enough power to deliver to other subsystems for the mission. Energy is stored using a battery pack. The solar arrays recharge the battery when facing the Sun, and the reaction wheels discharge the battery during maneuvers. The power available on the spacecraft is tightly coupled with the attitude discipline for each CubeSat. During the standby phase, the spacecraft orient themselves to charge their batteries using solar power.

Each battery cell is modeled by a Thevenin equivalent circuit model shown in Figure 8.

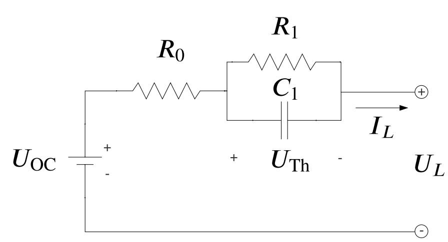

Figure 8 Equivalent circuit model of a battery cell using a Thevenin model with a single RC element.

The battery cell state of charge and voltage are modeled by

$$\begin{aligned} \dot{z}(t) &= \frac{I_L}{Q} \\ U_L &= U_{\mathrm{OC}} - U_{\mathrm{Th}} - I_L R_0 \end{aligned} \tag{13}$$

where z is the state of charge (SOC), Q is the cell capacity, I_L is the current, R_1 is the polarization resistance in the RC circuit, C_1 is the equivalent capacitance in the RC circuit, U_{OC} is the open-circuit voltage of the cell, R_0 is the internal resistance of the cell, and U_L is the voltage across the battery cell. Note that the battery cell itself is not an RC circuit, but the behavior of the cell is modeled by an equivalent circuit. The Thevenin voltage U_{Th} is modeled by the differential equation

$$\dot{U}_{\text{Th}} = -\frac{U_{\text{Th}}}{R_1 C_1} + \frac{I_L}{C_1} \tag{14}$$

The state of charge z is limited to be between 20% and 95%.

The values for the equivalent circuit model are computed using

$$U_{\text{OC}}, C_1, R_1 R_0 = f(z) \tag{15}$$

where f is a surrogate model generated from data for a lithium-ion battery provided by [32].

The battery pack current, voltage, and power are given by

$$\begin{aligned} I_{\text{bat}} &= I_L n_p \\ U_{\text{bat}} &= U_L n_s \\ P_{\text{bat}} &= I_{\text{bat}} U_{\text{bat}} \end{aligned} \tag{16}$$

where n_s and n_p are the number of battery cells connected in series, and number of battery cell series connected in parallel, respectively. The total number of battery cells in the battery pack is given by $n_s n_p$. The variables n_s and n_p are design variables in the optimization problem given by Table 4. The number of battery cells determines the mass and volume of the battery pack, which impacts the mass of the spacecraft and its energy capacity.

V. Optimization

The optimization problem is solved sequentially. The trajectory optimization problem is summarized in Table 3 and the attitude/battery sizing problem is summarized in Table 4. First, the trajectory optimization problem is solved over one orbit with the constraints shown in Figure 2 imposed on the relative positions of the two spacecraft. The objective of the first problem is to minimize thrust over the entire orbit. Constraints are enforced on the separation between the two spacecraft and the pointing error of the telescope. Then, the orbit from the trajectory optimization problem is fed into a second optimization that simultaneously optimizes the attitude profile and battery model. The objective of the second problem is to minimize the number of battery cells connected in series and in parallel. Constraints are enforced on the maximum torque applied by and power consumed by each reaction wheel, the minimum and maximum state of charge of the battery, and the

There are two scalar design variables per spacecraft; the number of battery cells connected in series, and the number of battery cells connected in parallel. Since these variables are integer design variables, a branch and bound method may be applied to solve a mixed-integer nonlinear program (MINLP). In this problem, these variables are treated as continuous variables and the solution is the lower limit of each variable. Since the scalar integer design variables are integers at the solution to the relaxed problem, the branch and bound method does not need to be applied in this particular study.

The model in all optimization problems simulates a single orbit, approximately 90 minutes, split into 301 time steps. The profile variables were discretized with 301 points and the time-dependent design variables were represented using fourth-order B-splines with 60 control points.

Table 3 Trajectory Optimization Problem

	Variable	Description	Quantity
Objective	$\sum_{i=1}^{2}(m_{\text{prop},0} - m_{\text{prop,f}})$	Total propellant mass used	
Design Variables	$-T_{max} \leq T(t) \leq T_{max}$	Thrust (omnidirectional)	$2{\times}3{\times}n_{\text{cp}}$ (a B-spline interpolation is used to obtain thrust for all time)
		Total no. of design variables	$6n_{\text{cp}}$
Constraints	$450 - h(t) \leq 0$	Altitude	2 (reduced from $2n_t$ using KS function)
			Continued on next page

Table 3 – continued from previous page

	Variable	Description	Quantity
	$(\lVert u^{(DSC)}(t) - u^{(\mathrm{OSC})}(t)\rVert - 40 - \varepsilon)LOS_s \leq 0$	Separation constraint (along LOS)	1 (reduced from n_t using KS function)
	$(40 - \varepsilon - \lVert u^{(DSC)} - u^{(\mathrm{OSC})}\rVert)LOS_s \leq 0$	Separation constraint (along LOS)	1 (reduced from n_t using KS function)
	$\lVert (u^{(\mathrm{OSC})}(t) - u^{(DSC)}(t)) \cdot \hat{r}_{sun}\rVert LOS_s - \varepsilon \leq 0$	Alignment constraint (in plane normal to LOS)	1 (reduced from n_t using KS function)
	$\lVert (u^{(\mathrm{OSC})}(t) - u^{(DSC)}(t)) \cdot \hat{r}_{sun}\rVert LOS_s - \varepsilon \leq 0$	Pointing constraint	1 (reduced from n_t using KS function)
		Total no. of constraints	6

Table 4 Attitude Profile and Battery Pack Optimization Problem

	Variable	Description	Quantity
Objective	$n_s n_p$	Total number of battery cells	
Design Variables	$0 \leq I \leq I_{sc,0}$	Solar power current	1
	$0.2 \leq z_0 \leq 0.95$	Initial state of charge	1
	$n_s \geq 1, n_p \geq 1$	Number of battery cells connected in series and in parallel	2
	$\phi_{B/I}(t), \theta_{B/I}(t), \psi_{B/I}(t)$	Spacecraft roll, pitch, and yaw in ECI frame	$3 \times n_{\mathrm{cp}}$ (a B-spline interpolation is used to obtain thrust for all time)
		Total no. of design variables	$4 + 3n_{\mathrm{cp}}$
Constraints	$0.2 - z(t) \leq 0$	State of charge	1 (reduced from n_t using KS function)
	$z(t) - 0.95 \leq 0$	State of charge	1 (reduced from n_t using KS function)
	$-\tau_{RW,max} - \tau_{RW}(t) \leq 0$	Reaction wheel torque along each axis	3 (reduced from $3 \times n_t$ using KS function)
	$\tau_{RW}(t) - \tau_{RW,max} \leq 0$	Reaction wheel torque along each axis	3 (reduced from $3 \times n_t$ using KS function)
	$I_{batt}(t) - 5 \leq 0$	Battery charge rate	1 (reduced from n_t using KS function)
	$-10 - I_{batt}(t) \leq 0$	Battery discharge rate	1 (reduced from $1n_t$ using KS function)
	$(1 - \varepsilon - (R_{B/I}^{(\mathrm{OSC})}(t)\hat{r}_{sun})_y)LOS_s \leq 0$	Optics spacecraft orientation	1 (reduced from n_t using KS function)
	$(1 - \varepsilon - (R_{B/I}^{(\mathrm{DSC})}(t)\hat{r}_{sun})_x)LOS_s \leq 0$	Detector spacecraft orientation	1 (reduced from n_t using KS function)

Continued on next page

Table 4 – continued from previous page

Variable	Description	Quantity
	Total no. of constraints	12

VI. Optimization Results

The optimization problem was defined in CSDL [21] to define the problems summarized in Tables 3 and 4, taking advantage of the fully automatic derivative computation using the adjoint method., and SNOPT [25], a reduced-Hessian active-set SQP solver to solve the optimization problems. We used the modOpt* framework as an interface between CSDL and SNOPT. Section VI.A presents the solution to the problem in Table 3 and Section VI.B presents the solution to the problem in Table 4.

A. Trajectory Optimization

The objective is to minimize total propellant used. The trajectory optimization converges to a feasibility of 10^{-5} and an optimality of 10^{-6}, (Figure 9). Figure 10 shows the positions of the Optics and Detector Spacecraft relative to the reference orbit after solving the problem summarized in Table 3. The positions of the spacecraft relative to the reference orbit at the solution is on the order of hundreds of meters.

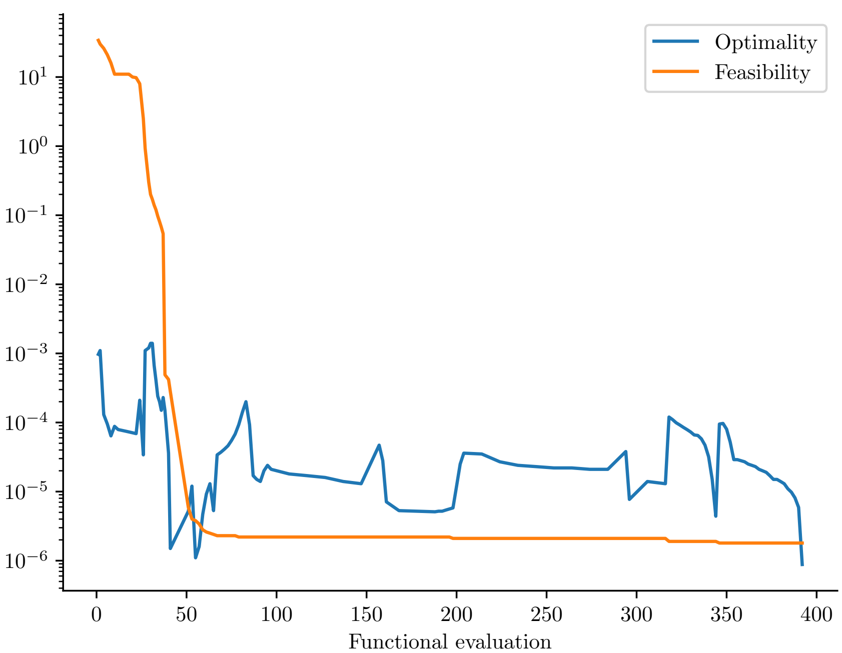

Figure 9 Convergence history for problem summarized in Table 3 using SNOPT.

*https://lsdolab.github.io/modopt/

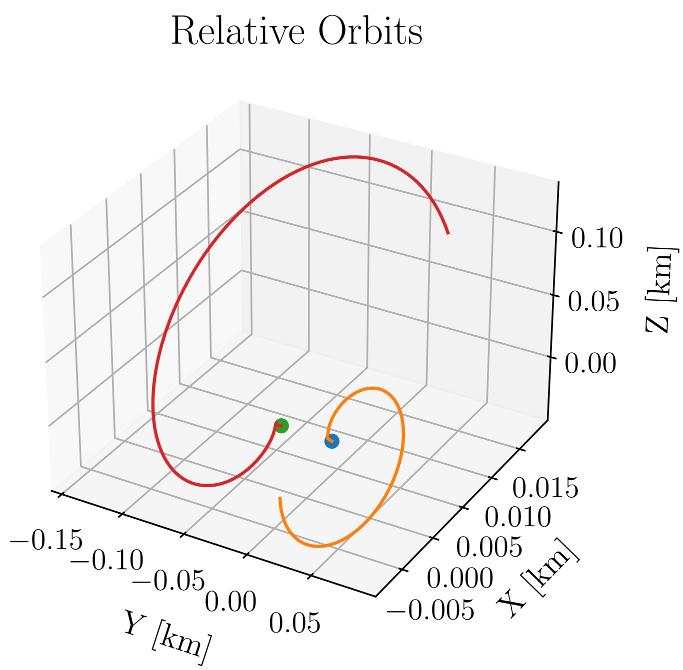

Figure 10 3D plot of relative orbits of both spacecraft relative to reference orbit at optimal solution of problem summarized in Table 3. Coordinates are in the Earth-Centered Inertial (ECI) frame of reference.

Figure 11 shows the values of the constraint variables on the telescope formation over time. The constraints are only enforced during the observation phase (highlighted in green). Figure 11 shows the successful optimization of the trajectory to satisfy the millimeter- and arcsecond-level constraints on the swarm formation.

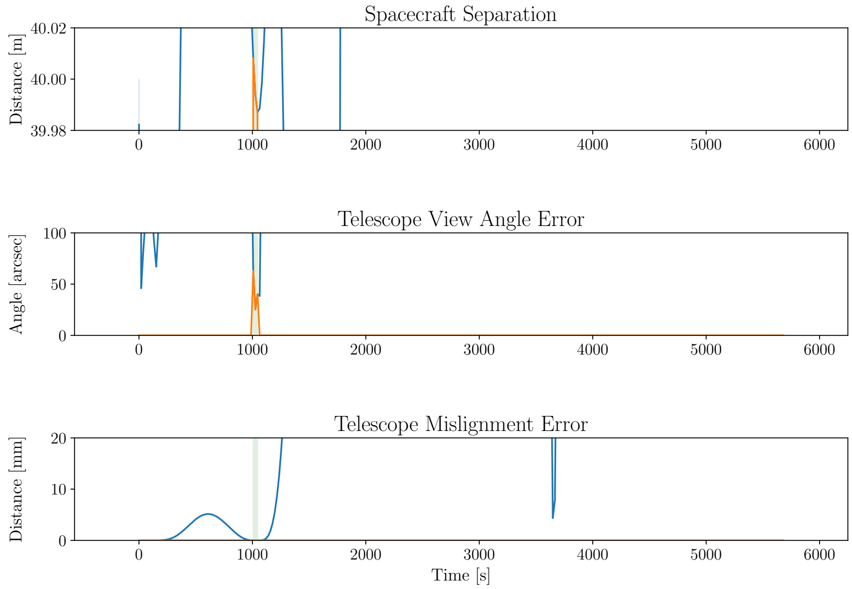

Figure 11 Telescope dimensions over one orbit. The green highlighted vertical strip indicates the observation phase of the orbit. The formation constraints are satisfied during the observation phase (separation is 40 m±15 mm, telescope pointing error is ≤90 arcsec, and telescope misalignment is ≤18 mm). The formation is maintained throughout the observation phase, which lasts for 38 s, exceeding the 10 s requirement.

Figure 12 shows the optimal thrust profile for both spacecraft. The thrust for both spacecraft varies the most prior to and during the observation phase and drops to zero for the rest of the orbit.

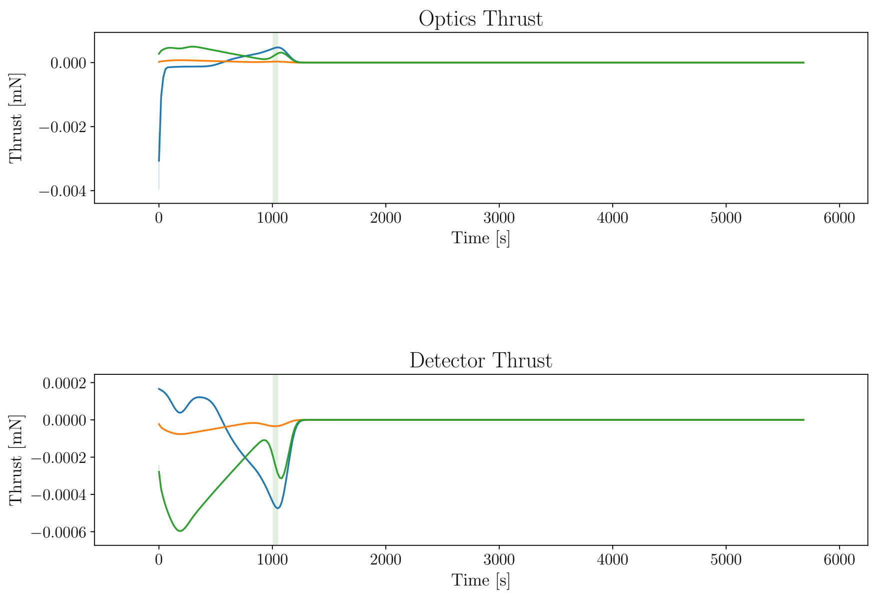

Figure 12 Thrust profile for each spacecraft over one orbit. Thrusters have omnidirectional capability and each component of thrust is in the Earth-Centered Inertial (ECI) frame of reference. The green highlighted vertical strip indicates the observation phase of the orbit.

Figure 13 shows the history of the values of the objective and aggregated constraint values for the trajectory optimization problem. The total propellant used starts at zero because the thrust variables are initialized to zero prior to the first function evaluation. The other constraint values are aggregated from time-dependent constraints using the KS function 1.

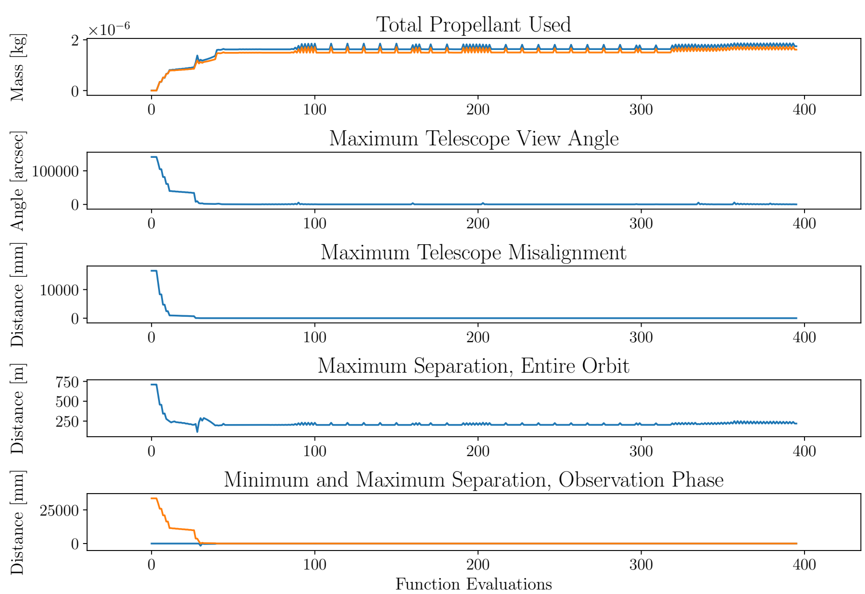

Figure 13 Objective and constraint history for trajectory optimization problem summarized in Table 3

B. Attitude Profile and Battery Pack Optimization

This section presents the solution to the problem summarized in Table 4. The orbit from the solution presented in Section VI.A is fed into in the problem summarized in Table 4. The problem is solved independently for each spacecraft, since the constraints imposed on the battery pack for each spacecraft depend only on the design variables for the same spacecraft. The attitude and battery pack optimizations converge to a feasibility of at most 10^{-4} and an optimality of at most 10^{-4}, (Figure 14).

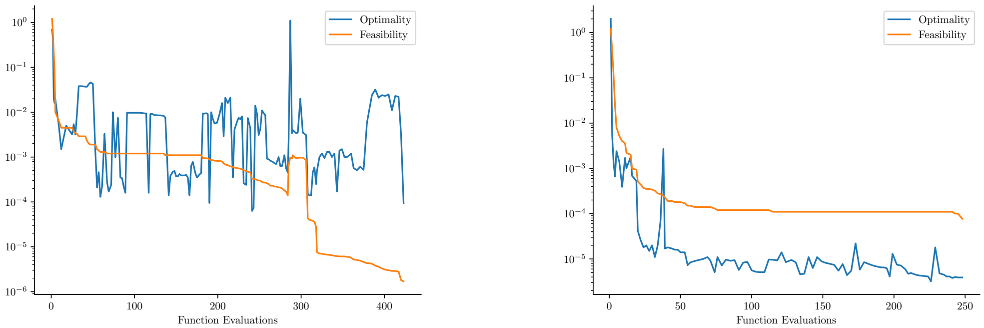

(a) (b)

Figure 14 Convergence history for problem summarized in Table 4 applied to (a) Optics Spacecraft and (b) Detector Spacecraft using SNOPT.

Figure 15 shows the roll, pitch, and yaw angles of the OSC and DSC at the solution, and the transition between the observation phase and standby phase of the orbit. The transition between observation phase and standby phase is more apparent in the Optics Spacecraft attitude profile because both spacecraft have the same initial guess for their respective attitude profiles, but different desired orientations during the observation phase (e.g. the orientation shown in Figure 3).

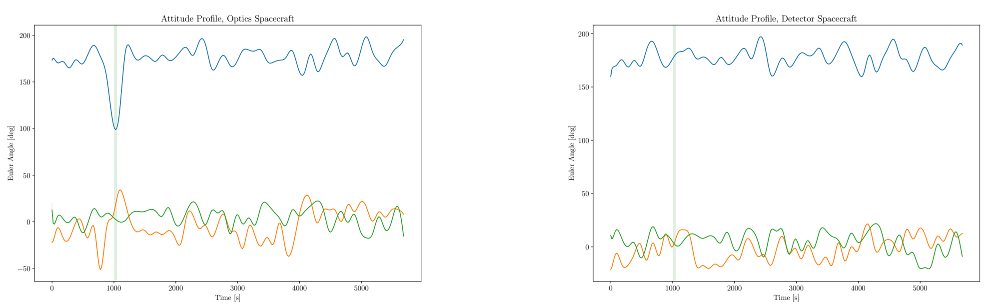

(a) (b)

Figure 15 Attitude profile of (a) Optics and (b) Detector Spacecraft as measured by roll, pitch, and yaw angles relative to Earth-Centered Inertial (ECI) frame after solving problem summarized in Table 4.

Figure 16 shows the percent of light from the Sun that reaches the telescope component throughout the orbit. During the observation phase, both spacecraft achieve an exposure of 98% or greater. The detector on the Detector Spacecraft is oriented towards the Sun for more of the orbit than the optics on the Optics Spacecraft is oriented toward the Sun. This is due to the fact that the optics and the detector are oriented differently relative to the solar arrays on each spacecraft, requiring a different orientation during the observation phase for each spacecraft.

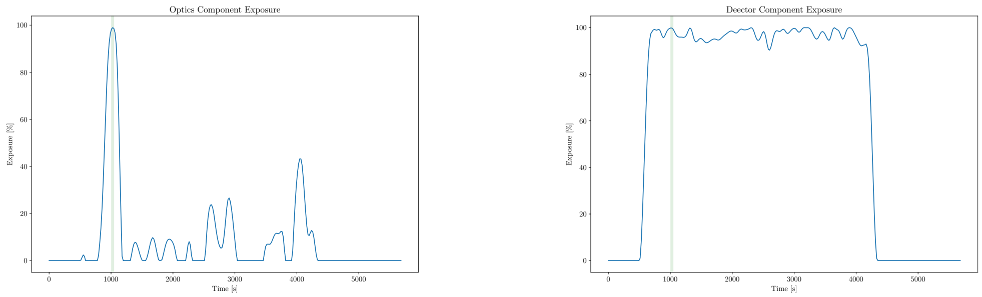

(a) (b)

Figure 16 Percent of light available for each instrument for (a) Optics and (b) Detector Spacecraft after solving problem summarized in Table 4. As the spacecraft points away from the Sun or enters Earth's shadow, the exposure to the Sun decreases.

Figure 17 shows the state of the battery pack onboard each spacecraft at the optimal solution. Both battery states of charge remain well above 20% and reach a maximum of 95%. The state of charge for both batteries decreases prior to the observation phase as both spacecraft reaction wheels consume power to achieve the desired orientation, and both spacecraft orient their solar arrays to drive the state of charge back to its value at the start of the orbit.

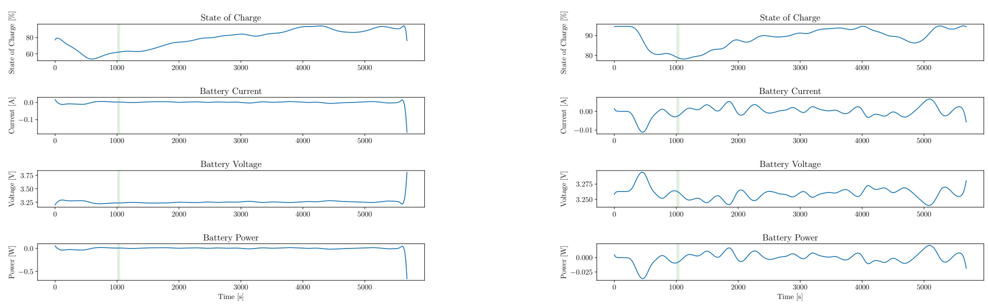

(a) (b)

Figure 17 Battery state of charge, current, voltage, and power for (a) Optics and (b) Detector Spacecraft after solving problem summarized in Table 4.

Figure 18 shows the reaction wheel speed, torque, and power over time at the solution. The reaction wheel speeds, the torque applied by the reaction wheels, and the power supplied to the reaction wheels do not have behaviors that show the observation phase and standby phase clearly. This indicates that the torque applied by the Earth's gravity field is a significant torque for the reaction wheels to counteract throughout the orbit.

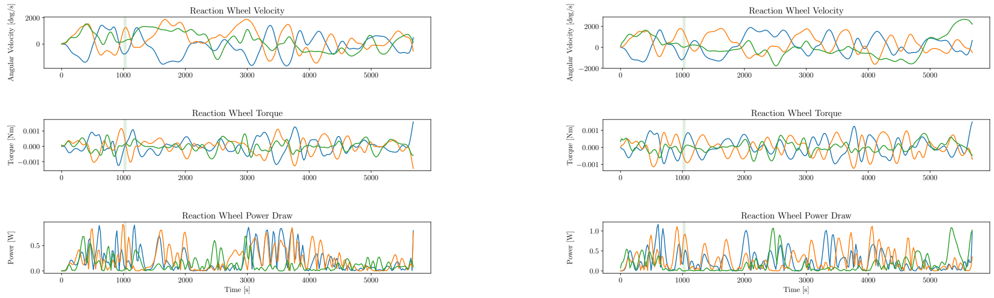

(a) (b)

Figure 18 Reaction wheel speed, torque and power for (a) Optics and (b) Detector Spacecraft after solving problem summarized in Table 4.

Figure 19 shows the state of the solar arrays for each spacecraft. The solar illumination, current, and voltage for the solar arrays on the Optics Spacecraft drop during the observation phase due to the fact that the optics and the detector are oriented differently relative to the solar arrays on each spacecraft, requiring a different orientation during the observation phase for each spacecraft.

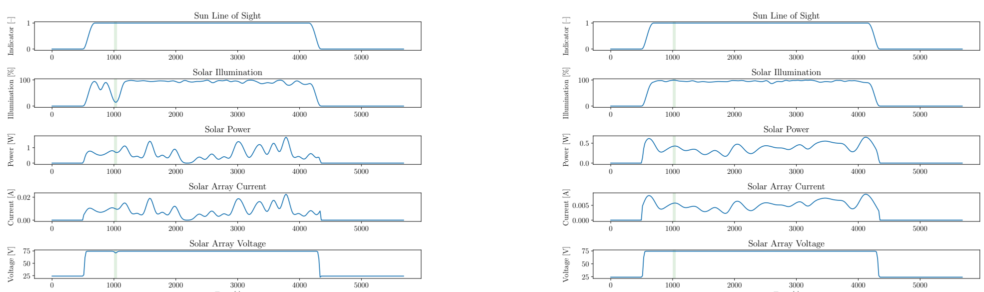

(a) (b)

Figure 19 Line of sight indicator and solar array illumination, power, current, and voltage for (a) Optics and (b) Detector Spacecraft after solving problem summarized in Table 4

VII. Conclusion

The objective of this study was to apply multidisciplinary design optimization (MDO) to the design of a virtual telescope comprised of two CubeSats. We used gradient-based optimization to optimize the trajectory, attitude profile, and battery sizing for each spacecraft. The key challenge was to satisfy constraints to millimeter-level accuracy when the positions of the CubeSats are on the order of thousands of kilometers. These large differences in orders of magnitude introduced truncation errors that render numerical optimization impossible. To enable numerical optimization, a relative orbit model was developed that avoids introducing truncation errors that would render numerical optimization impossible while also taking into account orbit perturbations.

The MDO problem was solved using a sequential approach, first solving the trajectory optimization problem for both spacecraft, and then using the solution in a subsequent optimization problem that simultaneously optimizes the attitude profile and battery pack. The successful design of a virtual telescope mission demonstrates MDO as a practical, scalable approach to solving spacecraft mission design problems involving swarms flying in formation.

Future work can take multiple directions. First, applying the methods developed in this paper to a swarm with a greater number of spacecraft will demonstrate the effectiveness of the orbit model developed in this paper. Second, increasing the number and fidelity of spacecraft subsystem disciplines will demonstrate the robustness of the approach used in this paper as well as the capability to perform optimization on later design iterations. Third, combining the trajectory, attitude profile, and sizing problems into one optimization problem and solving it simultaneously will demonstrate the robustness of the may lead to better local optimal solutions.

VIII. Funding Sources

This work was supported in part by the National Science Foundation under grant no. 1936557.

IX. Acknowledgments

References

[1] McCammon, D., and Kaaret, P., "XQCSAT: A High-Resolution Spectroscopic Study of Hot Gas in the Halo and Interstellar Medium," *American Astronomical Society Meeting Abstracts*, Vol. 234, 2019, pp. 108–05.

[2] Kaaret, P., McCammon, D., Nguyen, T., and Frank, D., "XQCSat-X-Ray Quantum Calorimeter Satellite," *The Space Astrophysics Landscape for the 2020s and Beyond*, Vol. 2135, 2019, p. 5007.

[3] Swartz, W. H., Lorentz, S. R., Huang, P. M., Reilly, S. M., Reilly, N. M., and Papadakis, S. J., "Radiometer assessment using vertically aligned nanotubes (RAVAN)," *IGARSS 2019-2019 IEEE International Geoscience and Remote Sensing Symposium*, IEEE, 2019, pp. 4975–4977.

[4] Cohen, B. A., Hayne, P. O., Greenhagen, B., Paige, D. A., Seybold, C., and Baker, J., "Lunar Flashlight: Illuminating the Lunar South Pole," *IEEE Aerospace and Electronic Systems Magazine*, Vol. 35, No. 3, 2020, pp. 46–52.

[5] Krieger, G., Moreira, A., Fiedler, H., Hajnsek, I., Werner, M., Younis, M., and Zink, M., "TanDEM-X: A satellite formation for high-resolution SAR interferometry," *IEEE Transactions on Geoscience and Remote Sensing*, Vol. 45, No. 11, 2007, pp. 3317–3341.

[6] Burns, R., McLaughlin, C. A., Leitner, J., and Martin, M., "TechSat 21: formation design, control, and simulation," *2000 IEEE Aerospace Conference. Proceedings (Cat. No. 00TH8484)*, Vol. 7, IEEE, 2000, pp. 19–25.

[7] Cheng, A., Michel, P., Reed, C., Galvez, A., Carnelli, I., and Headquarters, P., "Dart: Double asteroid redirection test," *European Planetary Science Congress*, Vol. 7, 2012, pp. 23–28.

[8] Rivkin, A. S., Chabot, N. L., Stickle, A. M., Thomas, C. A., Richardson, D. C., Barnouin, O., Fahnestock, E. G., Ernst, C. M., Cheng, A. F., Chesley, S., et al., "The double asteroid redirection test (DART): Planetary defense investigations and requirements," *The Planetary Science Journal*, Vol. 2, No. 5, 2021, p. 173.

[9] Macintosh, B., D'Amico, S., Koenig, A., and Madurowicz, A., "Miniature Distributed Occulter Telescope (mDOT): A Concept for a Smallsat Mission to Observe Extrasolar Zodiacal Dust and Exoplanets," *AGU Fall Meeting Abstracts*, Vol. 2019, 2019, pp. A43F–08.

[10] Pirayesh, R., Naseri, A., Moreu, F., Stochaj, S., Shah, N., and Krizmanic, J., "Attitude Control Optimization of a Two-CubeSat Virtual Telescope in a Highly Elliptical Orbit," *Space Operations: Inspiring Humankind's Future*, Springer, 2019, pp. 233–258.

[11] Rankin, K., Stochaj, S., Shah, N., Krizmanic, J., and Naseri, A., "VTXO: Virtual Telescope For X-ray Observations," *9th International Workshop on Satellite Constellations and Formation Flying*, 2017, p. 11.

[12] Park, H., Lee, Y., Lee, Y., Rankin, K., and Stochaj, S., "Design Optimization of a Space Virtual Telescope Mission Using a CubeSat Swarm," *70th International Astronautical Congress, Washington D.C.*, 2018.

[13] Llorente, J. S., Agenjo, A., Carrascosa, C., de Negueruela, C., Mestreau-Garreau, A., Cropp, A., and Santovincenzo, A., "PROBA-3: Precise formation flying demonstration mission," *Acta Astronautica*, Vol. 82, No. 1, 2013, pp. 38–46.

[14] Galano, D., Jollet, D., Mellab, K., Villa, J., Penin, L., Rougeot, R., and Versluys, J., "Proba-3 Precise Formation Flying Mission," *International Workshop on Satellites Contellations and Formation Flying (IWSCFF), Glasgow, United Kingdom*, 2019.

[15] Lightsey, E. G., Arunkumar, E., Kimmel, E., Kolhof, M., Paletta, A., Rawson, W., Selvamurugan, S., Sample, J., Guffanti, T., Bell, T., et al., "Concept of operations for the visors mission: A two satellite cubesat formation flying telescope," *AAS 22-125, 2022 AAS Guidance, Navigation and Control Conference*, 2022.

[16] Gundamraj, A., Thatavarthi, R., Carter, C., Lightsey, E. G., Koenig, A., and D'Amico, S., "Preliminary design of a distributed telescope cubesat formation for coronal observations," *AIAA Scitech 2021 Forum*, 2021, p. 0422.

[17] Koenig, A., D'Amico, S., and Lightsey, E. G., "Formation flying orbit and control concept for the VISORS mission," *AIAA Scitech 2021 Forum*, 2021, p. 0423.

[18] Martins, J. R., and Lambe, A. B., "Multidisciplinary design optimization: a survey of architectures," *AIAA journal*, Vol. 51, No. 9, 2013, pp. 2049–2075.

[19] Hwang, J. T., and Martins, J. R., "A computational architecture for coupling heterogeneous numerical models and computing coupled derivatives," *ACM Transactions on Mathematical Software (TOMS)*, Vol. 44, No. 4, 2018, pp. 1–39.

[20] Gray, J. S., Hwang, J. T., Martins, J. R., Moore, K. T., and Naylor, B. A., "OpenMDAO: An open-source framework for multidisciplinary design, analysis, and optimization," *Structural and Multidisciplinary Optimization*, Vol. 59, 2019, pp. 1075–1104.

[21] Gandarillas, V., Joshy, A. J., Sperry, M. Z., Ivanov, A. K., and Hwang, J. T., "A graph-based methodology for constructing computational models that automates adjoint-based sensitivity analysis," *Structural and Multidisciplinary Optimization*, (under review).

[22] Hwang, J., Lee, D. Y., Cutler, J., and Martins, J., "Large-scale MDO of a small satellite using a novel framework for the solution of coupled systems and their derivatives," *54th AIAA/ASME/ASCE/AHS/ASC Structures, Structural Dynamics, and Materials Conference*, 2013, p. 1599.

[23] Martins, J. R., and Hwang, J. T., "Review and unification of methods for computing derivatives of multidisciplinary computational models," *AIAA journal*, Vol. 51, No. 11, 2013, pp. 2582–2599.

[24] Poon, N. M., and Martins, J. R., "An adaptive approach to constraint aggregation using adjoint sensitivity analysis," *Structural and Multidisciplinary Optimization*, Vol. 34, No. 1, 2007, pp. 61–73.

[25] Gill, P. E., Murray, W., and Saunders, M. A., "SNOPT: An SQP algorithm for large-scale constrained optimization," *SIAM Rev.*, Vol. 47, 2005, pp. 99–131.

[26] Hwang, J. T., and Martins, J. R., "A fast-prediction surrogate model for large datasets," *Aerospace Science and Technology*, Vol. 75, 2018, pp. 74–87.

[27] *Reaction Wheels*, Blue Canyon Technologies, 2022. URL `https://storage.googleapis.com/blue-canyon-tech-news/1/2022/04/BCT_DataSheet_Components_ReactionWheels.pdf`.

[28] Gandarillas, V., and Hwang, J. T., "TALOS: A toolbox for spacecraft conceptual design," *arXiv preprint arXiv:2303.14936*, 2023.

[29] Hwang, J., "Efficient and scalable computational design of a small satellite," 2014.

[30] Kawamura, H., Naka, K., Yonekura, N., Yamanaka, S., Kawamura, H., Ohno, H., and Naito, K., "Simulation of I–V characteristics of a PV module with shaded PV cells," *Solar Energy Materials and Solar Cells*, Vol. 75, No. 3-4, 2003, pp. 613–621.

[31] Hwang, J. T., Lee, D. Y., Cutler, J. W., and Martins, J. R., "Large-scale multidisciplinary optimization of a small satellite's design and operation," *Journal of Spacecraft and Rockets*, Vol. 51, No. 5, 2014, pp. 1648–1663.

[32] Tran, M.-K., Mathew, M., Janhunen, S., Panchal, S., Raahemifar, K., Fraser, R., and Fowler, M., "A comprehensive equivalent circuit model for lithium-ion batteries, incorporating the effects of state of health, state of charge, and temperature on model parameters," *Journal of Energy Storage*, Vol. 43, 2021, p. 103252.